Title

Investigation of contact grid geometry for photon-enhanced thermionic emission (PETE) silicon based solar converters

Authors

Sandovsky, Rama
Segev, Gideon
Kribus, Abraham

Publication Date

2016-08-01

DOI

10.1016/j.solener.2016.03.066

Peer reviewed

Available online at www.sciencedirect.com

ScienceDirect

Solar Energy 133 (2016) 259–273

SOLAR ENERGY

www.elsevier.com/locate/solener

Investigation of contact grid geometry for photon-enhanced thermionic emission (PETE) silicon based solar converters

Rama Sandovsky [a], Gideon Segev [b], Abraham Kribus [a,*]

[a] School of Mechanical Engineering, Tel Aviv University, Tel Aviv 69978, Israel
[b] School of Electrical Engineering, Tel Aviv University, Tel Aviv 69978, Israel

Received 18 September 2015; received in revised form 9 March 2016; accepted 30 March 2016

Communicated by: Associate Editor D. Yogi Goswami

Abstract

Conversion of solar radiation to electricity with photon-enhanced thermionic emission (PETE) holds the theoretical promise of high conversion efficiency. Basic questions of converter materials properties and conversion process thermodynamics were addressed in recent work. Here we investigate two configurations of front and back electrical contacts on a silicon cathode, and the dependence of device efficiency on the contact area, using a two-dimensional detailed simulation. The impact of contact area on efficiency is different at moderate vs. high temperature, due to a change from electron recombination to electron injection at the contact. When the contact is small enough, a local potential gradient develops, which forms an effective barrier against electron recombination. The back contacts lead to higher efficiency compared to front contacts at all temperatures, and allow much higher contact area that may serve to reduce Ohmic loss and to absorb IR radiation.

Keywords: Thermionic emission; Solar electricity

1. Introduction

Thermionic emission converts heat to electricity by emission of electrons from the surface of a heated high temperature cathode, and their collection in a lower temperature anode (Hatsopoulos and Gyftopoulos, 1973). Appropriate treatment of both surfaces such that the work function of the cathode is higher than that of the anode leads to positive output voltage and output power. The electron flow through a thermionic converter is sustained by the temperature difference between the emitter and the collector, requiring heat addition at high temperature in the cathode and heat removal at the anode. Thermionic converters require cathode temperatures significantly above 1000 °C, and even at these high temperatures, their conversion efficiency is below 20%, and therefore they are not widely implemented.

In photon enhanced thermionic emission (PETE) converters, the cathode is made of a semiconductor material and is illuminated with above band gap photons, for example from concentrated sunlight (Schwede et al., 2010). Optical generation increases the concentration of conduction-band electrons in the cathode, and raises the conduction-band quasi-Fermi level. This reduces the effective barrier for electron emission, allowing electron emission at temperatures considerably lower than in standard thermionic emission. The excess photon energy above the band gap passes to the lattice through thermalization, leading to increased cathode temperature and

* Corresponding author.
E-mail address: kribus@tauex.tau.ac.il (A. Kribus).

http://dx.doi.org/10.1016/j.solener.2016.03.066
0038-092X/

Nomenclature

A	Richardson constant (A(cm K)$^{-2}$)
C	Auger recombination coefficient (cm^6 s^{-1})
d	gap size (μm)
E	energy (eV)
G	photo-generation rate (cm^{-3} s^{-1})
h	Planck's constant (eV s)
i	radiation spectral flux (W cm^{-2} μm^{-1})
$\overline{J}$	current density (A cm^{-2})
K_b	Boltzmann's constant (eV K^{-1})
L	cathode length (μm)
N_a^-	ionized acceptors concentration (cm^{-3})
N_d^+	ionized donors concentration (cm^{-3})
n	electron concentration (cm^{-3})
p	hole concentration (cm^{-3})
q	charge of an electron (C)
R	recombination rate (cm^{-3} s^{-1})
S	surface recombination velocity (cm s^{-1})
T	temperature (K)
t	contact finger half-width (μm)
V	operating voltage (V)
w	contact grid half-pitch (μm)
X	flux concentration ratio (—)

Greek symbols

α	volumetric absorption coefficient (cm^{-1})
λ	wavelength (μm)
ϵ_r	relative permittivity (—)
ν	frequency (s^{-1})
ϕ	work function (eV)
φ	quasi-Fermi potential (V)
σ	Stefan–Boltzmann constant (W m^{-2} K^{-4})
χ	electron affinity (eV)
Ψ	electric potential (V)
τ	life time (s)

Sub- and super-scripts

A	anode
BA	barrier for the anode
BC	barrier for the cathode
C	cathode
con	contact
eq	equilibrium
F	Fermi
g	bandgap
i	intrinsic
n	electrons
p	holes

higher emission current. Therefore, the PETE process converts some of the heat generated by thermalization into electrical power. The energy of sub-bandgap photons can also contribute to increase the temperature and the conversion efficiency, if the cathode contains an IR coupling element that absorbs them. The thermal contribution to the conversion process raises the PETE efficiency above the Shockley–Queisser limit for single junction solar cells, theoretically reaching around 50% (Schwede et al., 2010). Waste heat removed from the anode can drive a secondary heat-to-electricity converter stage, theoretically approaching overall efficiency of 70% under concentration of 1000 suns (Segev et al., 2015b).

Simple models of PETE conversion such as (Schwede et al., 2010; Segev et al., 2012) represented the cathode as a uniform lumped system. They did not account for spatial distributions within the cathode, and therefore can be called 'zero-dimensional'. Such models cannot represent the effect of realistic electrical contacts at the boundary of the cathode. A more elaborate one-dimensional model presented the spatial variations of charge carriers concentration and electrical potential across the cathode, and the differences in performance compared to the simpler zero-dimensional model (Segev et al., 2013). This work has shown the significance of modeling the electrical contact, demonstrating that contact surface recombination can cause a significant decrease in the PETE converter performance. A pp$^+$ junction under the contact, similar to the back surface field junction commonly used in photovoltaic cells, was analyzed as means to reduce this recombination loss. The effectiveness of this solution is not satisfactory, due to the reduction in the BSF barrier with the increase of the temperature, and due to the low p doping in the cathode bulk that is needed to obtain the junction. A hetero-junction was therefore proposed at the cathode contact as a better solution to repel electrons and reduce surface recombination. Hetero-junctions to block transport of electrons were used at both sides of the cathode (Schwede et al., 2013), and experimental results matched well with their model predictions. The junction near the emitting surface was designed not to completely block transport, but to filter the electrons population allowing only sufficiently energetic electrons to cross the thin emitter layer and reach the electron emission surface. The junction at the opposite side was used to completely block electrons and reduce surface recombination. Additional one-dimensional models for PETE converter were proposed, but they provided lower detail and neglected some important physical effects. One solved only the electron continuity equation and did not account for the distribution of the electric field and the hole concentration inside the cathode (Varpula and Prunnila, 2012), which may be important in

some cases. Another model accounted only for quantum efficiency and output current, and did not discuss net efficiency (Sahasrabuddhe et al., 2012). The representation of electrical contacts in all one-dimensional models is still not realistic: the contact is a completely transparent layer that covers the entire front surface of the cathode.

The significance of the cathode contacts is not only due to contact surface recombination, but also due to shading. A metallic electrical contact applied at the illuminated surface of the cathode should be constructed as a fine grid of strips ('fingers') that occupy a minimal area, similar to the practice in photovoltaic cells, in order to minimize the amount of shading. A model of the contacts must therefore account for the width and pitch of the grid fingers. Making the grid area too small can cause high series resistance ('Ohmic') loss, which is a serious concern in concentrating photovoltaic (CPV) cells due to the high concentration and high current densities (Nishioka et al., 2006). A similar concern applies to PETE converters that should operate under concentrated sunlight. For example, the short circuit currents in silicon PETE devices under 1000 suns can be about 100 A/cm^2 for a cathode operating at 800 K (Segev et al., 2013). Therefore, the grid geometry should be a compromise that balances these two effects of shading and resistance, similar to CPV cells.

It should be noted that the contact grid in a PETE cathode has an additional effect on performance, which is absent in PV cells. Radiation incident on the contact grid area cannot contribute to the photonic excitation in the cathode, but in principle, it can be thermally absorbed to contribute to heating of the cathode. An analysis of PETE contact grid geometry and its effect on performance should include this effect as well.

Another configuration that eliminates shading altogether is to put the contacts at the back of the device, and keep the entire front surface exposed to the incident radiation. This works well and improves performance in back-contact PV cells (Van Kerschaver and Beaucarne, 2006). Applying the same approach in PETE converters may pose some interesting challenges. First, a contact grid at the back surface of the cathode occupies an area intended for electron emission. This could reduce the emitted current and therefore reduce the conversion efficiency. Therefore, the width and pitch of the contact grid fingers are also important in this configuration. Second, the thickness of the contact should be smaller than the vacuum gap size, to avoid an electrical and thermal bridge from the cathode to the anode. This gap should normally be very small – around 3 μm – to avoid the detrimental effect of negative space charge (Segev et al., 2015a).

In this work, we investigate the impact of contact geometry on the performance of a PETE cathode and converter, considering the effects of shading, electron recombination at the contact surface, and thermal effects. A two-dimensional simulation of a PETE converter is employed to model metallic contacts with specified width and spacing at the surface of the cathode. This investigation applies to both front surface and back surface contacts.

2. Analysis

2.1. Model setup and geometry

Fig. 1 shows a schematic of the PETE cathode geometry. A representative section of the cathode is modeled as a two-dimensional problem, assuming no variations in the device structure, properties, and the incident radiation in the third direction. Fig. 1(b) shows the front contact configuration, where the electrical contact grid is located at the illuminated absorber surface $y = L$, the contact 'finger' width is $2t$, and the grid pitch is $2w$. The emitting surface is located at $y = 0$, and reflection symmetry applies at $x = 0$ and $x = w$. Fig. 1(c) shows the alternate configuration of back contacts, where the electrical grid is located on the electron emission surface. The vacuum gap and the anode are not modeled explicitly, and they are included in the model via the boundary conditions, as discussed below.

The assumptions used in the analysis include:

- Two-dimensional problem: all variables are uniform in the third direction.
- Incident sunlight is collimated.
- The cathode temperature is uniform.
- Charge transport through the boundary occurs at the contact surface only, representing both surface recombination and charge transport to/from the contact. Other cathode surfaces are ideal.
- Photon recycling within the cathode is not considered.
- The electrical resistance of the contact grid is neglected.
- Space charge in the vacuum gap is not considered.
- The anode is perfectly conductive and perfectly reflective to radiation.

Some of these assumptions are highly idealized, and in real materials and devices the neglected effects can have a significant impact on performance. However, this is consistent with, and enables comparison to, previous analyses that made the same assumptions; and it is expected that trends found here will be valid in real devices, even if the absolute value of efficiency will be different due to various effects that were neglected.

2.2. The governing equations

2.2.1. Transport of charge carriers

The analysis follows in general the method of Segev et al. (2013), except that the problem here is two-dimensional instead of one-dimensional. The continuity equations describe the transport of charge carriers within the cathode (Sze and Kwok, 2006), and are given here in terms of quasi Fermi potentials:

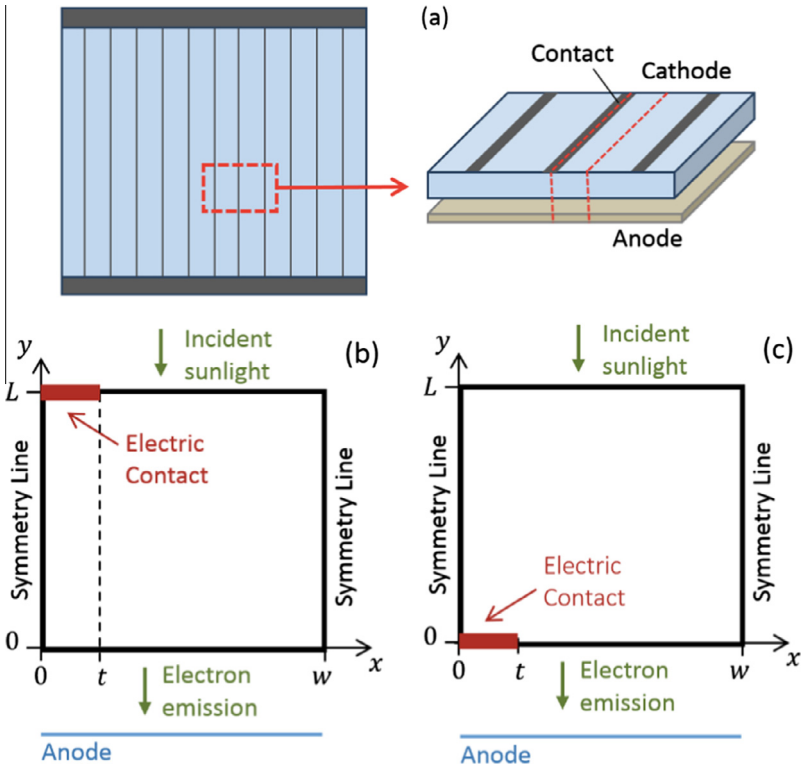

Fig. 1. (a) Schematic of PETE converter, (b) two-dimensional model geometry of a section of the PETE cathode, front contact grid configuration and (c) back contact configuration.

$$\overline{\nabla}(\mu_n n \overline{\nabla}\varphi_n) = (G - R) \tag{1}$$

$$\overline{\nabla}(\mu_p p \overline{\nabla}\varphi_p) = -(G - R) \tag{2}$$

G is the photo-generation, and R is the total recombination, per unit volume. μ_n and μ_p are the electron and hole mobilities, n and p are the electron and hole carrier densities. The quasi-Fermi potentials for electrons φ_n and for holes φ_p are related to the charge carriers' concentrations:

$$\varphi_n \equiv \Psi - \frac{K_b T_C}{q} \ln\left(\frac{n}{n_i}\right) \tag{3}$$

$$\varphi_p \equiv \Psi + \frac{K_b T_C}{q} \ln\left(\frac{p}{n_i}\right) \tag{4}$$

q is the electron charge, n_i is the intrinsic equilibrium concentration of electrons, Ψ is the electric potential, K_b is Boltzmann's constant and T_C is the cathode temperature. The distributions of electrons and holes can then be expressed in terms of quasi Fermi potential and the electric potential:

$$n = n_i \cdot \exp\left[\frac{q(\Psi - \varphi_n)}{K_b T_C}\right] \tag{5}$$

$$p = n_i \cdot \exp\left[\frac{q(\varphi_p - \Psi)}{K_b T_C}\right] \tag{6}$$

The current densities of electrons and holes in terms of the quasi Fermi potentials are:

$$\overline{J}_n = -qn\mu_n \overline{\nabla}\varphi_n \tag{7}$$

$$\overline{J}_p = -qp\mu_p \overline{\nabla}\varphi_p \tag{8}$$

The electric potential within the cathode depends on the distribution of charge carriers' concentrations by Poisson's equation (Sze and Kwok, 2006):

$$\nabla(\epsilon \overline{\nabla}\Psi) = q(N_a^- - N_d^+ + n - p) \tag{9}$$

N_a^- and N_d^+ are the ionized acceptors and donors concentrations, and ϵ is the permittivity. Since the PETE device operates at high temperature, all the donors and acceptors are considered to be ionized. The set of equations for the electric potential and charge carriers' quasi Fermi potentials is solved over a section of the cathode, as shown in Fig. 1, given a distribution of the photo-generation and the appropriate expressions for recombination.

2.2.2. Generation

We assume for simplicity that the incident light is collimated, even though concentration of sunlight always produces a large range of directions. The absorption is then exponential for each wavelength with the normal penetration distance into the cathode. The distribution of photo-generation in the cathode for incident radiation with a one-sun spectral flux $i(\lambda)$ and concentration ratio X is then:

$$G(y; T_C) = X \cdot \int_0^{\lambda(E_g)} \alpha(\lambda; T_C) \cdot i(\lambda) \cdot \frac{\lambda}{hc} \cdot e^{-\alpha(\lambda;T_C)\cdot(L-y)} d\lambda \tag{10}$$

$\alpha(\lambda; T_C)$ is the semiconductor spectral absorption coefficient, which can depend on the cathode temperature. For wavelengths above the value corresponding to the cathode bandgap, the value of α is practically zero.

For the cathode configuration where the electrical contact is at the front surface, as shown in Fig. 1(b), two options were used. The generation profile of Eq. (10) applies for an ideal transparent contact that does not interact with the incident radiation. For a more realistic contact that blocks the incident radiation, the generation was set to zero in the cathode area under the contact, i.e., $x < t$, while the profile of Eq. (10) holds in all other locations.

2.2.3. Recombination

The total recombination rate per unit volume is the sum of rates of three recombination mechanisms:

$$R = R_{rad} + R_{Auger} + R_{SRH} \tag{11}$$

The radiative recombination rate per unit volume follows:

$$R_{rad} = \left(\frac{n \cdot p}{n_i^2} - 1\right) \cdot \int_0^\infty \frac{8\pi v^2}{c^2} \frac{\alpha(v; T_C)}{e^{\frac{hv}{k_b T_C}} - 1} dv \tag{12}$$

The actual rate of radiative recombination includes also the square of the index of refraction (Wurfel, 2005), but this is absent here, since only this part of the emitted photons is lost by leaving the cathode's external surface. The difference in index of refraction between the semiconductor and the air causes internal reflection, and reflected photons will be re-absorbed within the cathode to create new electron–hole pairs, an effect usually called 'photon recycling'. An accurate representation of this internal transport mechanism requires the solution of the radiative transfer equation in parallel to the current model, which is beyond the scope of this work. Here we use a simple approximation where only the net rate of recombination is represented as shown in Eq. (12). This corresponds to case III of Martı et al. (1997), where (1) the device is assumed to have interfaces to air or vacuum at both sides, and (2) the optical thickness for emitted photons within the critical angle cone is low, so they will not be reabsorbed before reaching the surface. The radiative recombination loss with photon recycling due to reflection at the external interfaces, represented by the device reverse saturation current under dark conditions, is calculated in Martı et al. (1997) using the index of refraction of the *external* medium rather than the emitting medium. This is consistent in the integral detailed balance of charge carriers and energy for the entire device. In our case, the integral balance is valid, but the spatial distribution of charge carrier generation will be skewed. The approximation of using Eq. (12) is equivalent to the assumption that photons emitted by radiative recombination, and unable to leave the cathode due to reflection at the interface, are reabsorbed at the same location of the original emission. In reality of course the reabsorption will take place over the entire cathode volume. For all cases in the current study the magnitude of the radiative recombination loss, calculated at the maximum power point according to Eq. (12) and integrated over the entire cathode, was limited to around 3% or less relative to the rate of generation (Sandovsky, 2015). Based on the difference between Eq. (12) and the exact expression for local radiative recombination, we estimate that recycled photons that redistribute charge carriers over the cathode should amount to about 30% of the overall generation rate. In our simulations, the distribution of electrons concentration over the cathode does not show large gradients except near surfaces with high surface recombination (Sandovsky, 2015), even though the generation profile varies greatly between the front and back surfaces. This indicates that the electrons are redistributed effectively by diffusion and drift even without the photon recycling mechanism. Neglecting the internal redistribution effects of this mechanism should then be acceptable.

Another form of photon recycling occurs for the photons that are emitted toward the anode, are reflected, and make another pass through the cathode with the possibility of absorption. We neglect the absorption of these reflected photons, with the understanding that this is a conservative approximation that lowers the resulting conversion efficiency. Nevertheless, according to the previous estimate these photons should amount to only 1.5% or less compared to the generation rate, so this effect is not very significant.

The Auger recombination rate depends on the density of both electrons and holes (Van Zeghbroeck, 2011):

$$R_{Auger} = C_n\left(n^2 p - n_{eq}^2 p_{eq}\right) + C_p\left(p^2 n - p_{eq}^2 n_{eq}\right) \tag{13}$$

C_n and C_p are Auger recombination coefficients for electrons and holes, respectively. The Shockley–Read–Hall (SRH) recombination rate is (Van Zeghbroeck, 2011):

$$R_{SRH} = \frac{np - n_{eq}p_{eq}}{\tau_n(p + n_i) + \tau_p(n + n_i)} \tag{14}$$

τ_n and τ_p are the charge carriers SRH life times for electrons and holes.

2.3. Boundary conditions

2.3.1. The electric contact surface

The Fermi level of the semiconductor and the metallic electric conductor is equal at the interface, and the contact permits the transport of both electrons and holes. We use the model of effective surface recombination for electrons and holes, which is appropriate when the two materials have the same work function (Sze and Kwok, 2006):

$$\hat{n} \cdot \overline{J}_n = -qS_n(n - n_{eq}) \tag{15}$$

$$\hat{n} \cdot \overline{J}_p = qS_p(p - p_{eq}) \tag{16}$$

$\hat{n}$ is a unit vector normal to the surface, S_n and S_p are the surface recombination velocities for electrons and holes at the contact surface, and n_{eq} and p_{eq} are the equilibrium concentrations at the surface. Setting the surface

recombination velocity for electrons to zero $S_n = 0$ in Eq. (15) represents a perfect selective barrier that completely blocks recombination of electrons, and this serves as a model for an ideal hetero-junction with a high barrier for electrons.

Ohmic resistance loss in the electric contact itself is not considered, and therefore the electric potential at the contact is uniform and is set as zero:

$$\Psi = 0 \tag{17}$$

2.3.2. The electron emission surface

The emitting surface should have reasonably low electron affinity, in order to reduce the energy barrier to electron emission. The usual means to achieve low or even negative electron affinity is to apply a specific coating, such as alkali metals and their oxides (Hatsopoulos and Gyftopoulos, 1973) or a thin layer of polycrystalline diamond with hydrogen termination (Mearini et al., 1994). The boundary condition here does not represent the details of the coating, only its effect to reduce the electron affinity, and it assumes no other effects of the coating such as surface recombination or Ohmic resistance.

The potential gradient at the emission surface is proportional to the electric field in the gap between the electrodes, which depends on the operating voltage. This field can be found from summation of all potential differences in the electrical circuit that contains the cathode, gap and anode:

$$-\epsilon_r \frac{\partial \Psi}{\partial \hat{n}} = \frac{\hat{n}}{d}\left[(\phi_A + V) - \left[E_g + \chi - q(\Psi - \Psi_{con}) - E_{f,C}\right]\right] \tag{18}$$

d is distance between cathode and anode, ϵ_r is the relative permittivity, ϕ_A is the anode work function, V is the external operating voltage of the PETE converter, E_g and χ are the cathode bandgap and electron affinity, respectively. Ψ_{con} is the electric potential at the contact surface, and $E_{f,C}$ is the cathode's Fermi level.

The cathode's electron emission surface supports transport of electrons only, and no transport of holes, under the assumption stated above of an ideal surface with no recombination. The net current density for electrons is the balance of the emitted current, and the reverse current of electrons that are emitted from the anode and reach the cathode (Segev et al., 2012). The boundary conditions on current density are then:

$$\hat{n} \cdot \overline{J}_n = J_{em} + J_{rev} \tag{19}$$

$$\hat{n} \cdot \overline{J}_p = 0 \tag{20}$$

The emission from the cathode accounts only for electrons that have enough energy to reach the anode:

$$J_{em} = -qnv_n \cdot e^{-\frac{\chi + E_{BC}}{k_b T_C}} \tag{21}$$

v_n is the average velocity of an emitted electron in the direction normal to the cathode surface. E_{BC} is the additional energy barrier that an electron emitted from the cathode needs to overcome, in order to reach the anode. For voltages below the saturation voltage (the value of the external voltage where the vacuum levels of the cathode and anode are the same), the electric field at the surface is negative, accelerating electrons toward the anode, and this barrier is therefore zero:

$$E_{BC} = \begin{cases} 0 & \partial\Psi/\partial n > 0 \\ -\epsilon_r d \cdot \partial\Psi/\partial n & \partial\Psi/\partial n \leqslant 0 \end{cases} \tag{22}$$

The reverse current from the anode is:

$$J_{rev} = AT_A^2 \cdot e^{-\frac{\phi_A + E_{BA}}{k_b T_A}} \tag{23}$$

A is Richardson's constant, T_A is the anode temperature, and ϕ_A is the anode work function. E_{BA} is the additional energy barrier that electrons emitted from the anode need to overcome, in order to reach the cathode. For voltages above the saturation voltage, the electric field in the gap (and at the cathode surface) is positive, accelerating electrons toward the cathode, and this barrier is therefore zero:

$$E_{BA} = \begin{cases} \epsilon_r d \cdot \partial\Psi/\partial n & \partial\Psi/\partial n > 0 \\ 0 & \partial\Psi/\partial n \leqslant 0 \end{cases} \tag{24}$$

Fig. 2 shows the energy barriers for electron emission in the two cases where the operating voltage is below and above the saturation voltage.

2.3.3. The absorber surface

Following the assumption of ideal surfaces with no recombination, there are no currents passing through the absorber surface, and the electric field is equal to zero at this surface:

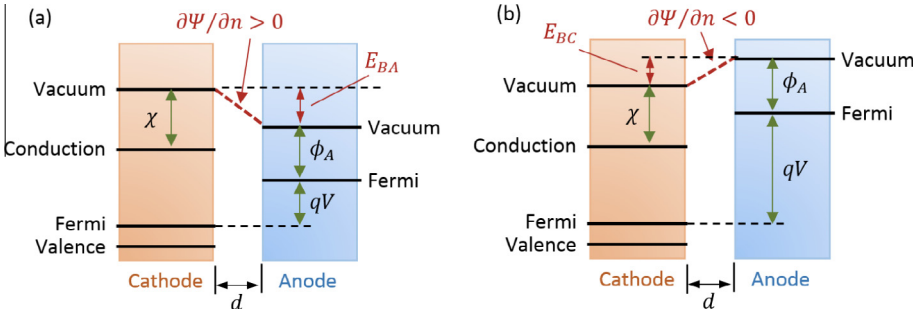

Fig. 2. Energy barriers for electrons emitted from the cathode and anode (a) voltage lower than saturation voltage and (b) voltage higher than saturation voltage.

$$\hat{n} \cdot \overline{J}_n = 0 \tag{25}$$

$$\hat{n} \cdot \overline{J}_p = 0 \tag{26}$$

$$\frac{\partial \Psi}{\partial \hat{n}} = 0 \tag{27}$$

2.3.4. The symmetry surfaces

At the boundaries $x = 0$ and $x = w$, the symmetry condition implies zero current crossing the surface, and a zero normal derivative of the potential. These boundary conditions are identical to Eqs. (25)–(27) that apply at the absorber surface.

2.4. Energy balance

So far, the cathode temperature value was set arbitrarily. In reality, an energy balance on the cathode will determine its steady state temperature (Segev et al., 2012). The incident radiation power P_{in} equals the sum of all power transfers that leave the cathode by different paths: radiation, conduction, and advection with emitted electrons.

$$P_{in} = P_{el} + P_{rad} + P_{IR} + P_{con} + P_{cond} \tag{28}$$

P_{el} is the power transported by electrons from the cathode to the anode, and is calculated as the net current times the energy carried by an electron:

$$P_{el} = \int_0^w (J_{em} + J_{rev})dx \cdot (E_C - E_F + \chi + E_{BC}) \tag{29}$$

In the back contact configuration, the integral over electron emission area is from t to w. P_{rad} is the power loss due to net radiative recombination:

$$P_{rad} = \int_0^w \int_0^L \frac{n \cdot p}{n_i^2} dy\, dx \cdot \int_0^\infty \frac{8\pi v^2}{c^2} \frac{\alpha(v; T_C) \cdot hv}{e^{\frac{hv}{k_B T_C}} - 1} dv \tag{30}$$

Discussion of total vs. net radiative recombination rates was given in Section 2.2.3 above. This expression accounts for emitted photons that not recycled, i.e., they reach the cathode surfaces at an angle below the critical angle and are able to exit the cathode (Martı et al., 1997). Eq. (30) applies when both surfaces, including the contact, are transparent. When the contact is opaque, a fraction of P_{rad} proportional to the contact area is blocked, while the contact itself can emit blackbody radiation instead.

P_{IR} is the radiation power emitted from the IR coupling element, a perfect selective absorber that absorbs all incident sub-bandgap radiation (Schwede et al., 2010). The power emitted by this element is:

$$P_{IR} = \frac{w \cdot 2\pi}{h^3 c^2} \int_o^{E_g} \frac{(hv)^3}{e^{hv/k_B T_C} - 1} d(hv) \tag{31}$$

P_{con} is the radiative power loss due to the presence of the contact at the front surface. Two types of ideal optical behavior of the contact are considered here. For a transparent contact there is no loss: $P_{con} = 0$. For a black contact, the incident radiation is fully absorbed, but there is a loss by blackbody emission from the contact: $P_{con} = t \cdot \sigma T_C^4$. In this case, the losses due to radiative recombination and IR emission are reduced by a factor of $(1 - t/w)$, due to absorption of emitted photons at the inner side of the contact.

P_{cond} is power removed from the cathode by thermal conduction. In an ideal model, the cathode is thermally isolated, i.e., $P_{cond} = 0$. In any real implementation, however, the cathode will have some mechanical mounting and electrical connection components, and there will be some heat loss by conduction through these components: $P_{cond} > 0$. The cathode temperature in the ideal case is the highest possible temperature, and any heat loss by conduction will cause a reduction in the cathode temperature. This work considers only an ideal thermally isolated cathode.

2.5. Numerical solution and validation

The PETE converter model was implemented in *COMSOL Multiphysics* 4.3 and solved numerically. Solving the set of equations of Section 2.2 with the relevant boundary conditions and fixed values of the voltage and temperature yields a single operating point of the device. Varying the operating voltage yields a complete *I–V* curve of the device, leading to identification of the maximum power point and device efficiency. Coupling Eq. (28) to the previous set of equations allows solving simultaneously for the cathode temperature in the ideal thermally isolated case. Consistency of the numerical solution was verified by varying the numerical mesh density, until changes in the solution were less than 0.8%. In addition, the total current was calculated separately as an integral of the current density at both sides of the cathode, yielding equal results.

Full validation of this model is not possible, since no relevant experimental results exist, and no previous two-dimensional model of the PETE converter exists for comparison. We have compared results of the two-dimensional model to those of a previous one-dimensional model (Segev et al., 2013). Fig. 3 shows the comparison of *I–V* curves at different cathode temperatures, for a problem with a transparent electric contact

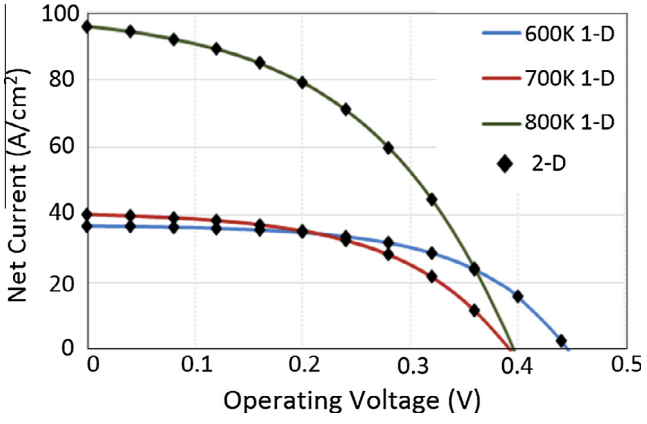

Fig. 3. Comparison of the two-dimensional model results to those of a one-dimensional model from Segev et al. (2013).

covering the whole front of the cathode. The excellent correspondence to the results of the one-dimensional model shows consistency of the present 2-D model with previously published work.

3. PETE performance with front contacts

3.1. Converter definition

The results shown here are for cathodes made of silicon. Table 1 shows the material properties. The spectral absorption coefficient for Si as function of temperature was calculated according to (Weakliem and Redfield, 1979), based on the absorption coefficient at 300 K taken from Green and Keevers (1995). The acceptor doping at the cathode was 10^{17} cm^{-3}, except for cases with a pp^{+} junction as a barrier next to the contact: in these cases, the cathode bulk doping was 10^{12} cm^{-3}, and the barrier layer was doped 10^{19} cm^{-3}. Table 2 shows the PETE converter geometry, where the half-width of the contact finger t is a free parameter. The grid pitch w was selected based on a study of CPV cells, where the optimal pitch at 1000 suns was found to be around 100 μm (Nishioka et al., 2006). Changing the conductor width t, while holding the grid half-pitch w constant, results in changing the fraction of the cathode area that is covered by the contacts. The anode work function was set at an optimistic value of 0.5 eV, expecting that ongoing efforts may be successful to develop advanced coatings that reduce surface work function below the currently reported value of 0.9 eV (Koeck et al., 2009). The incident radiation was the AM1.5D spectrum, multiplied by a concentration ratio of 1000 suns for all the simulations. The additional parameters of the PETE converter shown in Table 2 are also common to all cases analyzed here.

Table 2
PETE converter geometry, device properties and operating conditions.

Property	Symbol	Value
Cathode length	L	100 μm
Contact grid half-pitch	w	60 μm
Concentration ratio	X	1000
Emitting surface electron affinity	χ	0.1 eV
Anode work function	ϕ_A	0.5 eV
Anode temperature	T_A	500 K

3.2. Shading by the contact

The front contact grid has two major effects addressed here: shading a part of the active area of the cathode from the incident radiation, and recombination at the contact surface. For a better understanding, it can be helpful to isolate the electronic effect from the optical effect. In this section we consider the effect of shading on the converter performance, by setting the contact boundary condition to a perfect selective barrier (Section 2.2.3) that prevents electron recombination. The charge generation profile is changed according to the contact half-width t, as explained in Section 2.2.2.

Fig. 4 shows the internal quantum efficiency, defined as the rate of electrons emitted from the cathode to the anode at short circuit condition, normalized to the total photogeneration in the cathode that would occur with a transparent contact (no shading). The contact half-width t is

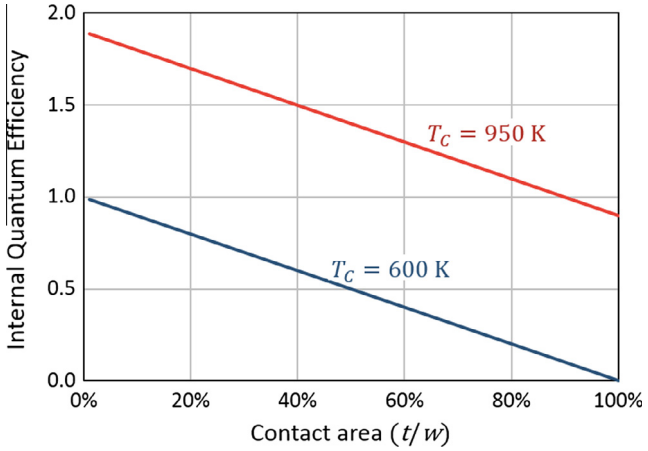

Fig. 4. Internal quantum efficiency as function of the front contact fractional area for different cathode temperatures. The contact is an ideal barrier to electrons, all parameters are according to Table 2.

Table 1
Properties of the silicon cathode.

Property	Symbol	Value
Electron mobility (Lombardi et al., 1988)	μ_n	1400 m^2/V s
Hole mobility (Lombardi et al., 1988)	μ_p	470 m^2/V s
Relative permittivity (Neamen, 2003)	ϵ_r	11.68
Electron surface recombination velocity at the contact (Rosenwaks et al., 1990)	S_n	10^6 cm s^{-1}
Hole surface recombination velocity at the contact (Rosenwaks et al., 1990)	S_p	10^6 cm s^{-1}
Auger recombination constant for electrons (Dziewior and Schmid, 1977)	C_n	$2.8 \cdot 10^{-31}$ cm^6 s^{-1}
Auger recombination constant for holes (Dziewior and Schmid, 1977)	C_p	$1.2 \cdot 10^{-31}$ cm^6 s^{-1}
Life time for electrons (ASTM, 1993)	τ_n	1 ms
Life time for holes (ASTM, 1993)	τ_p	1 ms
Band gap (Fan, 1986)	E_g	$E_g(T_C) = 1.170\ \text{eV} - \frac{4.73 \cdot 10^{-4}\ \text{eV K} \cdot T_C^2}{T_C + 636\ \text{K}}$
Cathode acceptor doping	N_a^-	10^{12} cm^{-3} for pp$^+$ homo-junction 10^{17} cm^{-3} for other cases

varied from 1% to 100% (full coverage) of the half-pitch w. All other parameters are as defined in Table 2. At low cathode temperature $T_C = 600$ K, the quantum efficiency is very close to the fraction of the area exposed to illumination. There is no recombination at the contact, bulk recombination is relatively low, and almost all of the generated electrons participate in emission toward the anode.

For higher temperature in the cathode, $T_C = 950$ K, the curve slope is the same, but the quantum efficiency values are higher, compared to the lower temperature. This is a result of operation in the thermionic emission regime (Segev et al., 2013). The values of quantum efficiency higher than one show the dominant role of the thermal mechanism: in this case, the electrons concentration in the cathode is depleted to less than the equilibrium concentration, and electrons are generated thermally regardless of the incident radiation. Under these conditions, the emission current consists of a photonic component that is very similar to the emission at lower temperature, and a thermal emission component, which does not depend on the contact size.

3.3. Surface recombination at the contact

To consider the effect of contact recombination without shading, we set the contact to be perfectly transparent. The case when the contact width is equal to the grid pitch ($t = w$) is equivalent to the one-dimensional model (Segev et al., 2013). Fig. 5(a) shows the internal quantum efficiency as a function of the contact size at low cathode temperatures $T_C = 550$ K. The acceptors concentration at the cathode is uniform at 10^{12} cm^{-3} without a junction next to the contact, and all other parameters are as in Table 2. For large contacts, the efficiency is low due to high recombination at the contact. The right inset in Fig. 5(a) shows electron flow paths for a contact covering 50% of the front surface, where about half of the photo-generated electrons flow toward the contact instead of the emitting surface.

For smaller contacts, the quantum efficiency can exceed one. This cannot be a result of thermal generation, due to the low cathode temperature. The mechanism that provides here additional electrons, beyond the amount of photogeneration, is injection of electrons from the contact, due to a potential difference that develops under the contact. Near the narrow contact, the current density of holes is high, leading to high Ohmic potential drop near the contact, as seen in Fig. 5(b) for a contact that covers 5% of the area. This effect is much smaller for larger contact area. The strong local electric field causes a depletion of electrons below the equilibrium concentration near the contact, leading to injection of electrons from the contact to the cathode. The left inset in Fig. 5(a) shows electron trajectories for a 5% contact, where injection from the contact is clearly visible, leading to an increase in the amount of electrons available for emission beyond the rate of photogeneration. For smaller contact sizes of 1% or less, electron injection from the contact still exists, but the smaller area produces a smaller total injection current, and the effect is not large enough to raise the quantum efficiency above one. In any case, when the contact is small enough, the loss by recombination at the contact disappears. The local potential gradient near the contact creates an effective barrier for electrons and there is no need for a junction to prevent surface recombination.

For higher cathode temperatures, the cathode operates in the thermionic regime. The high thermionic emission current leads to depletion of electrons over the entire cathode, resulting in electron injection at the contact as well as thermal generation in the bulk of the cathode. As a result, the model predicts quantum efficiency higher than one for the whole range of contact sizes at the higher temperatures.

3.4. I–V characteristics

Fig. 6 shows the current–voltage and power–voltage diagrams for a cathode with 10% contact area, and a pp$^+$

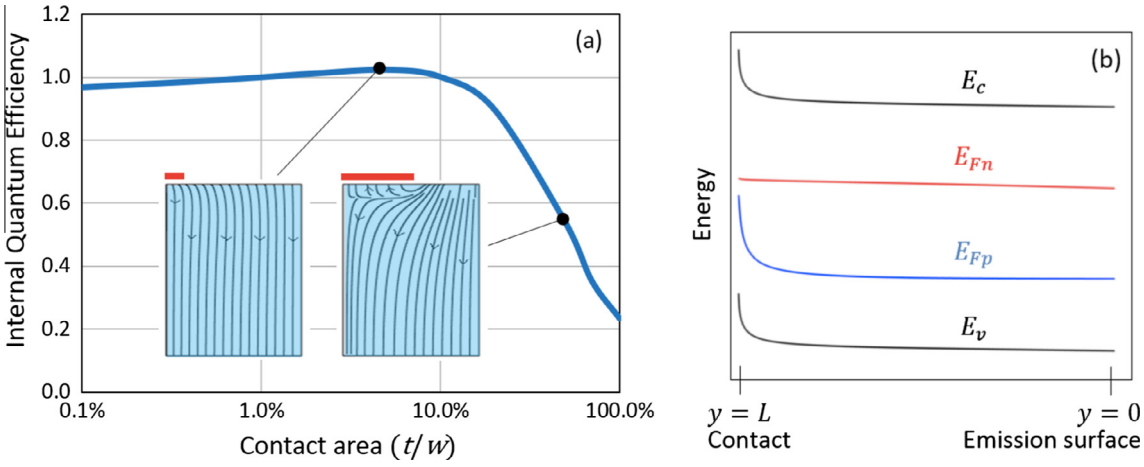

Fig. 5. (a) Internal quantum efficiency as a function of the contact size for a cathode at 550 K with a transparent contact and no junction. Insets: electron flow paths for 5% and 50% contact area. (b) Energy band diagram for the 5% contact at $x = 0$.

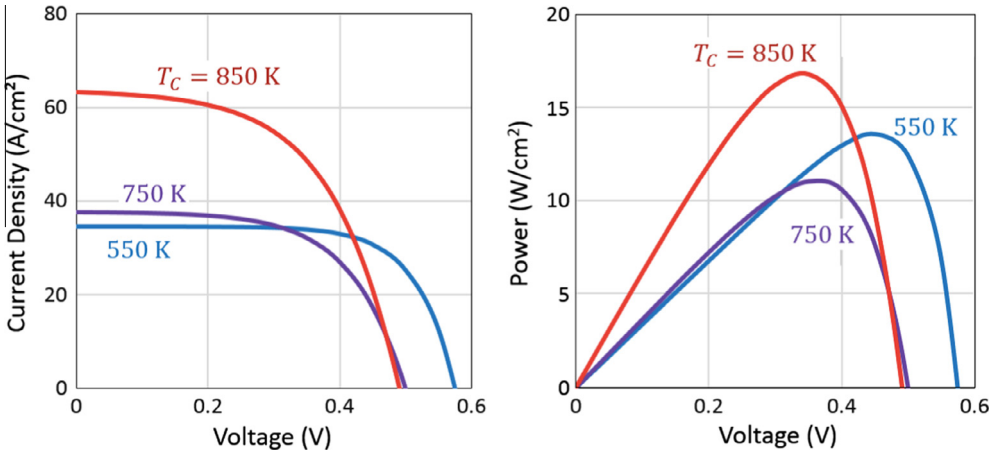

Fig. 6. Current–voltage and power–voltage characteristics for contact coverage of 10% at different temperatures. The cathode has a pp^+ homo-junction at the contact, all parameters are according to Table 2.

homo-junction at the contact surface as a barrier to electron recombination (which may be needed at lower temperatures). The effect of increasing the cathode temperature is similar to that observed in PV cells, even though the mechanisms are different. The short circuit current increases with temperature, with a small increase from 550 K to 750 K, and a much larger increase from 750 K to 850 K. This is consistent with the nonlinear dependence of saturation current on temperature in thermionic emission, which is the dominant effect at the higher temperatures. The open circuit voltage decreases with temperature between 550 K and 750 K, mostly due to the degradation of the homo-junction potential difference as the temperature increases. Further change as temperature increases to 850 K is very small. Other phenomena, such as the change of the material's bandgap with temperature, also have an effect but it is secondary. The net result of the two major effects is that the maximum power output of the PETE device has a minimum as a function of temperature: at 750 K it is lower than at 550 K, due to the drop in voltage. At higher temperature, further change in voltage is small, the increase in current becomes dominant, and the power output increases. This behavior is similar to that reported previously using the 1-D model with a transparent contact covering completely the front surface (Segev et al., 2013). The presence of a finite and more realistic contact does not change then the general behavior of the power output as a function of cathode temperature.

3.5. Efficiency and maximum temperature

Fig. 7 shows the efficiency of the PETE converter as a function of temperature for different sizes of the contact. The contact is black, the cathode has a homo-junction below the contact, and all other parameters are according to Table 2. The efficiency for each contact size decreases slightly with temperature in the PETE regime of moderate temperatures, following the trend discussed in the previous section, and then increases sharply at the onset of the

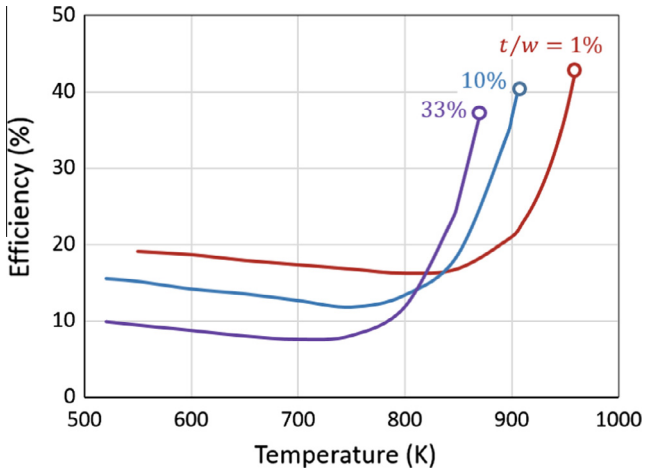

Fig. 7. Efficiency as function of cathode temperature for different contact sizes. Circles are the maximum achievable temperatures under ideal thermal balance. Contacts are black with a pp^+ homo-junction.

thermionic regime. The circle in each case indicates the maximum cathode temperature that is attained with an ideal energy balance, i.e., no loss by thermal conduction. All other points at lower temperatures in each curve imply a certain amount of conduction heat loss, or intentional heat removal, from the cathode. Obviously, these maximum temperatures are based only on an energy balance, and do not account for any temperature limitations of real materials.

At low cathode temperatures, the efficiency increases with a decrease in the contact size. The smaller contact reduces the shading loss, and reduces the possibility of recombination of electrons at the contact. Operation in this regime produces lower efficiency compared to the higher temperatures, and it might make sense when subject to the temperature limitations of real materials. For a given temperature limit in this range, the cathode design then favors smaller contacts. This is similar to the design of CPV cells, which is also driven by the need to minimize

shading by the contact grid. At higher cathode temperatures, the device operates in the thermionic regime and larger contacts are better for each given temperature. As discussed above, in this range of temperatures the larger contacts can inject more electrons into the cathode, in excess of the photo-generated electrons. Hence, for a given temperature in this range, the current and the efficiency increase with the contact size.

It is interesting to note that a converter with a larger contact will reach ideal thermal balance at a lower operating temperature, compared to the thermal balance with a smaller contact. Consequently, the highest maximum efficiency under ideal thermal balance is with the smaller, rather than the larger, contacts. The reason for this reversal is that in the thermionic regime, the maximum power point current increases with contact size due to injection of electrons from the contact in excess of the photo-generated electrons. Fig. 8(a) shows this increase in MPP current density at thermal balance as a function of increase in the contact size. The increased current does not, however, produce higher output power, due to the concurrent decrease in the MPP voltage, also shown in Fig. 8(a). Fig. 8(b) shows that the useful electrical output decreases with an increase in contact size.

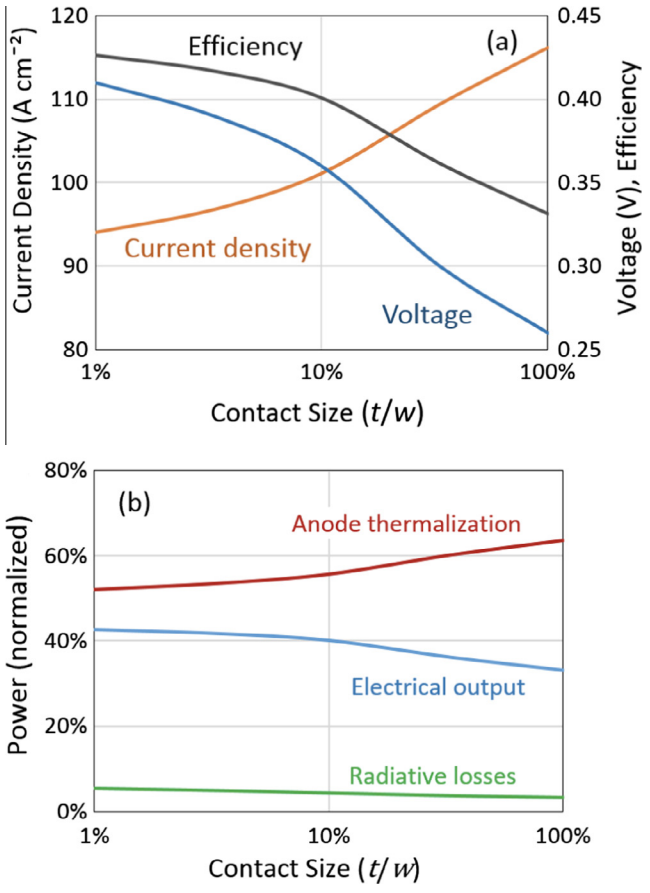

Fig. 8. (a) Maximum power point voltage, current and efficiency at thermal balance condition as function of the contact size. (b) Energy balance components: electrical output, anode thermalization, and cathode radiative losses, at thermal balance condition as function of the contact size.

Fig. 8(b) shows the division of the incident power into electrical output, radiative loss from the cathode, and thermalization loss in the anode. Thermalization in the anode is clearly the leading loss mechanism, even though we used a very low anode work function. This loss accounts for more than 50% of the incident power, while radiative losses from the cathode are much smaller. This is due to the high current density that occurs at the thermal balance condition: emitted electrons remove a significant amount of energy from the cathode, with a significant part of this energy ending as thermalization loss in the anode. Therefore, the higher current in the large contact device leads to lower ultimate cathode temperature and lower efficiency at ideal thermal balance. It is also remarkable that smaller contacts at thermal balance reach higher temperatures, which should have led to higher, rather than lower, current density. This indicates that the restriction by the contact size of electron injection from the contact is a stronger effect, compared to the increase of thermionic emission with temperature.

Fig. 9 shows the efficiency vs. temperature with a small contact of 1% area for three different types of contact: the ideal selective contact that blocks all transport of electrons, the contact with pp$^+$ homo-junction, and the simplest contact without the junction. Also shown is the 1-D solution (Segev et al., 2013) for a Si cathode with a homo-junction and the same parameters, except that the contact is transparent and covers the entire area. At moderate temperatures, the efficiency of the simple cathode with no junction is lower due to recombination at the contact, while the homo-junction acts almost like the ideal barrier in preventing recombination to reach higher efficiency. Even the case without any barrier at the contact is better than the

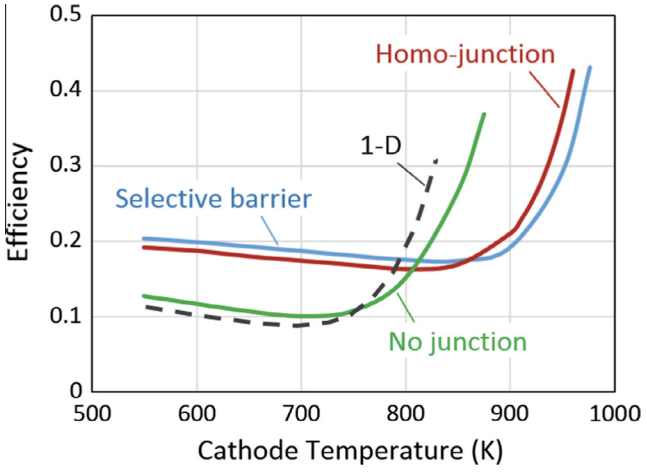

Fig. 9. Efficiency as function of cathode temperature for three types of contacts, all with 1% area: ideal selective barrier, pp$^+$ homo-junction, and no junction; and the 1-D full area contact (Segev et al., 2013). For the selective barrier and no junction the acceptor concentration is 10^{17} cm^{-3}, while for the homo-junction case the cathode acceptor concentration is 10^{12} cm^{-3}. All other properties are according to Table 2.

1-D case, because the small size of the contact forms an effective barrier as discussed above, and reduces recombination more effectively than the homo-junction applied to the full-area contact of the 1-D case.

At higher temperatures in the thermionic regime, the simple cathode increases its performance rapidly with electron injection from the contact into the depleted cathode. The homo-junction cathode also increases in efficiency but at higher temperatures. The highly doped layer of the junction near the contact reduces electron injection into the cathode, and a significant increase in current and efficiency is then delayed to higher temperatures. The case of the ideal barrier requires the highest temperature to achieve high efficiency, since it is not capable of electron injection from the contact, and the increase in current occurs only by thermal generation in the bulk of the cathode at higher temperatures.

4. PETE performance with back contacts

4.1. Back vs. front contact

A PETE converter with an electric grid located at the back of the cathode, as shown in Fig. 1(c), will have the entire cathode front surface open to illumination, eliminating the shading loss. However, this is not the only effect. The transfer of the electric contact from the front to the back of the cathode can impact the electron contact recombination in two opposite ways. On the one hand, the larger distance of the contact surface from the area of photo-generation can lead to a decrease in the recombination at the contact. On the other hand, the reduction in the electron emission area may cause an increase in the electron concentration within the cathode, and this can lead to an increase in recombination. We compare the two cases with back and front electric grids, for a homogenous cathode without a junction so that electron recombination at the contact can be a significant loss mechanism. In order to create the same photo-generation in both cases, the front contacts are transparent.

Fig. 10(a) shows the internal quantum efficiency as defined above in short circuit operation for two cathodes, with a 10% area contact at the front and back of the cathode. At cathode temperature of 600 K the back contact has more than 90% quantum efficiency, while its front contact counterpart is below 60%. The difference becomes even larger at higher cathode temperatures. The recombination at the contact should then be much higher in the front contact case. This is clearly visible in Fig. 10(b), where electron flow paths for the front contact configuration show clearly that nearly half of the electrons photo-generated near the front surface of the cathode end up in the contact. For the back contact case, only a small fraction of electron flow lines end at the contact surface. For the higher temperature, a similar examination of the electron flow paths (not shown) indicates that the injection of electrons from the back contact into the depleted cathode is more effective

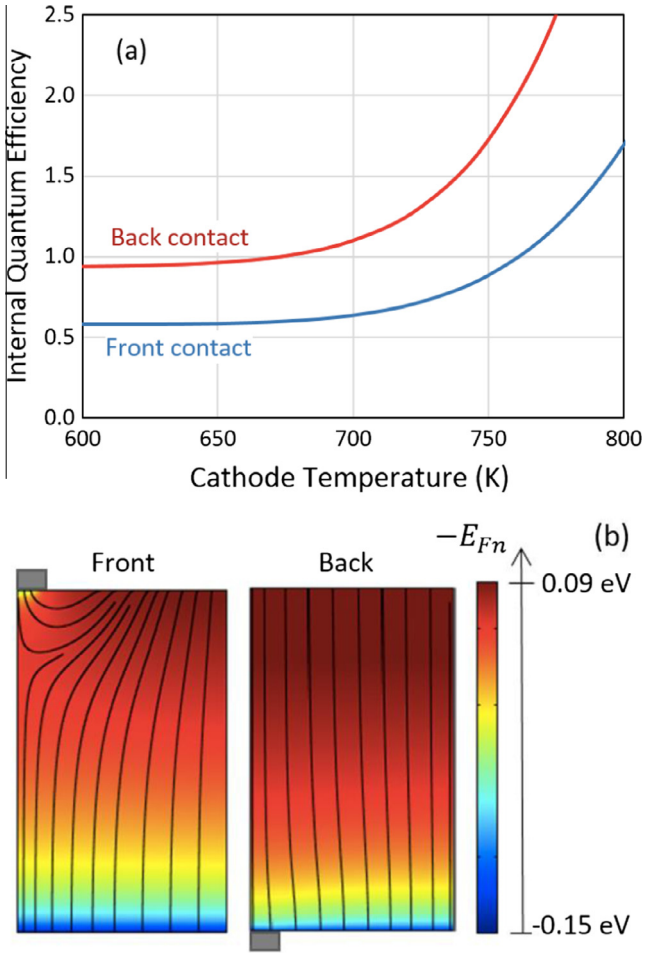

Fig. 10. (a) Internal quantum efficiency at short circuit as a function of cathode temperatures for 10% front and back contacts. The front contacts are transparent, all other properties are according to Table 2. (b) Electron flow paths and quasi-Fermi level for the front and back contact cases at 600 K.

compared to the front contact. For example, at cathode temperature of 750 K the front contact is still causing recombination loss, while the back contact is already injecting additional electrons at the same temperature. The lower electron concentration near the back surface, and the shorter path for injected electrons to reach the emission surface, seem to be the beneficial factor for the better performance of the back contact cathode.

4.2. Conversion efficiency vs. contact size

Fig. 11 shows the PETE converter efficiency as a function of the cathode temperature for a range of back contact sizes. Dashed lines in Fig. 11 are the 10% and 33% front contact cases from Fig. 7. The contacts are equipped with a pp^+ junction and all other data is according to Table 2. The behavior of the back contact cases as a function of temperature, and as a function of contact size for a given temperature, is similar to that of the front contacts. However, comparing the front and back contacts of the

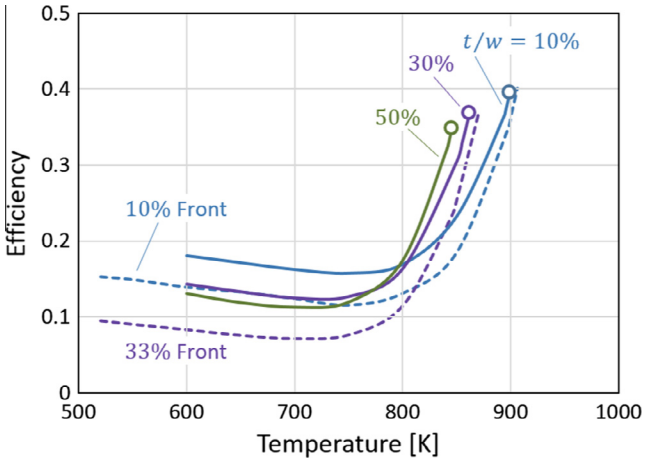

Fig. 11. Efficiency as a function of the cathode temperature, for different sizes of back contact (solid lines) and front contact (dashed lines). Circles are the maximum achievable temperatures under ideal thermal balance. Contacts are black with a pp^+ homo-junction.

same size, it is clear that the efficiency with back contacts is significantly higher. Moreover, the efficiency with a 33% front contact is much lower even when compared to the larger 50% back contact. The back contact configuration has then better performance, and allows using larger contacts with a smaller penalty, compared to the front contact configuration.

4.3. IR Coupling with back contacts

Back contacts intercept any incident radiation that is not absorbed in the cathode. Therefore, the contact may also be utilized as a partial IR coupling element that absorbs sub-bandgap photons, without interference with the absorption of supra-bandgap photons. This is a first suggestion for a specific implementation of IR coupling, which was mentioned in previous theoretical studies (Segev et al., 2012, 2013) only as an abstract concept. The previously shown result that back contacts may have a large area without a large penalty in efficiency enables interception and absorption of a large fraction of the IR photons.

In order to understand the potential benefit that can be added with this mechanism, we calculated the fractions of solar energy that are absorbed and transmitted through a 100 μm-thick layer of Si as a function of the temperature. Due to its relatively low band gap, Si absorbs above-bandgap photons accounting for more than 90% of the incident solar radiation power for temperatures above 650 K, and 94% at 1000 K where the bandgap is even lower. The contact absorbs all incident photons according to its area, and affects the maximum temperature that can be reached in thermal balance condition. The result for a 50% contact is that using the contact for absorption of transmitted photons increases the conversion efficiency by 1.6% at thermal balance, compared to the same contact with a reflective surface. For a 10% contact, the increase in efficiency due to absorption at the contact is only 0.5%. These are fairly small increases in efficiency. However, for other cathode materials that have bandgap near the optimal value, i.e., near 1.4 eV at operating temperature, less than 70% of the incident solar energy will be absorbed in the cathode. Then the addition of IR coupling at the contact can have a much higher impact on conversion efficiency.

5. Conclusions

This work is the first to consider the issue of contact grid geometry for a PETE converter. We have shown that the arrangement of the contacts has a significant impact on the converter performance, and therefore the contacts configuration should be carefully optimized. The contacts can affect performance in several ways: shading (in front contacts), recombination loss at the contact surface, injection of electrons into the cathode (when electrons population is depleted), and IR coupling (in back contacts). The optical effects of shading and IR coupling are fairly straightforward. Shading by front contacts is proportional to the fraction of area occupied by the contact. It has a significant impact in the PETE regime, similar to the shading in PV cells, but a lesser impact in the thermionic regime where photonic excitation makes a relatively smaller contribution. IR coupling at the back contact is also proportional to the contact area, and its impact depends the cathode bandgap.

The recombination of electrons at the contact can be a significant loss when operating at moderate temperatures in the PETE regime, similar to PV cells. Consistent with previous work, we have shown that a pp^+ junction, or a hetero-junction, can serve as a barrier that repels electrons from the contact, similar to a back-surface field (BSF) junction in photovoltaic cells. At higher temperatures, however, high emission current leads to depletion of electrons in the cathode, and the effect is reversed. The contact injects electrons into the cathode, instead of removing them, and there is no need for the barrier. The two-dimensional simulation presented here revealed another situation that limits recombination, based on geometry rather than on temperature. When the contact is small, the high current density of holes creates a potential gradient near the contact, causing local depletion of electrons and injection of electrons from the contact even at moderate temperatures. In this case as well, there is no need for an additional barrier to prevent recombination, and the geometric effect of contact size is sufficient to prevent recombination loss. Removal of the junction can lead to considerable simplification in the structure of the cathode. Another aspect that should be taken into account, however, is that a junction at the contact can increase the operating voltage of the device, even if it is not needed to prevent contact surface recombination. The inclusion of a junction in the cathode design should therefore be considered regarding all aspects of performance vs. complexity.

In the thermionic regime at the high temperature range, the thermionic mechanism dominates over the photonic excitation, and the contacts inject electrons into the cathode. Therefore, for a given temperature in the thermionic regime it is beneficial to increase the contact size and allow a higher injection current. For most materials there will be some limit on permitted operation temperature, and if this temperature is in the thermionic operation regime, then larger contacts can increase the conversion efficiency, in spite of the increase in shading. The external surface of the contact needs to be black in order to absorb the incident radiation as thermal energy. When the contact covers the entire front area, the device becomes a pure thermionic converter.

The back contact configuration has a consistent advantage over front contacts with the same area over the entire temperature range. This is true even for large contacts that occupy much of the cathode surface and reduce significantly the area available for electron emission. This is very beneficial in several ways: larger contacts reduce Ohmic losses, the contact may be used effectively to capture a large part of the IR radiation, and shading is completely eliminated. Implementation of this cathode configuration will be an interesting technical challenge, as it needs to fit in the narrow vacuum gap, while avoiding any electrical or thermal shorts between the cathode and anode.

One of the optimistic assumptions in this analysis is the lack of space charge in the inter-electrode gap. In real devices, negative space charge due to high electrons density in the gap has a major impact on the net current and device efficiency, leading to a requirement of a very small gap (Segev et al., 2015a). In the front contact configuration, it is likely that the effects of the contacts geometry and the space charge are independent. However, in the back contact configuration proposed here the grid may interact with the electrons in the gap. Based on the simulations that were performed without a space charge model, the electrostatic potential at the contact should be lower than at the electron emission surface (Sandovsky, 2015), so that a local electric field in the vicinity of the contact will tend to drive the emitted electrons away from the contact. In any case, the cloud of emitted electrons occupies a rectangular space with width that is one or two orders of magnitude larger than its height, and therefore any loss of electrons due to interaction with the contact at the sidewall of this space should be minimal. However, this aspect deserves a deeper analysis as part of a full investigation of space charge effects.

The results shown here are specific to the particular material properties of Si as cathode. The low absorption coefficient due to the indirect bandgap, and the high diffusion length, lead to a relatively thick cathode and enable a large distance between grid fingers. In other cathode materials, for example of the III–V group, both the absorption length and diffusion length will be much shorter, and the cathode design should have a much thinner active layer and shorter distances between contacts. Also, the relative contributions of the different bulk recombination mechanisms can be different, for example a much higher fraction of radiative recombination in direct bandgap materials. However, while taking these differences into account, we can postulate that the impact of surface recombination at the contacts will still be significant, and the same trade-offs regarding contact area fraction and contact location will be relevant to other materials as well. This needs of course to be verified by detailed investigation and separate optimization for each candidate cathode material.

Acknowledgment

Support for this work was provided by the Israel Ministry of National Infrastructure, Energy and Water.

References

ASTM, ASTM F28-91 Standard, 1993. In: Annual Book of ASTM Standards, vol. 10.05, ASTM, p. 30.

Dziewior, J., Schmid, W., 1977. Auger coefficients for highly doped and highly excited silicon. Appl. Phys. Lett. 31 (5), 346–348.

Fan, J.C.C., 1986. Theoretical temperature dependence of solar cell parameters. Sol. Cells 17, 309–315.

Green, M.A., Keevers, M.J., 1995. Optical properties of intrinsic silicon at 300 K. Prog. Photovoltaics Res. Appl. 3 (3), 189–192.

Hatsopoulos, G.N., Gyftopoulos, E.P., 1973. Thermionic Energy Conversion Volume I: Processes and Devices. MIT Press, Cambridge, MA, USA.

Koeck, F.A.M., Nemanich, R.J., Lazea, A., Haenen, K., 2009. Thermionic electron emission from low work-function phosphorus doped diamond films. Diam. Relat. Mater. 18 (5–8), 789–791.

Lombardi, C., Manzini, S., Saporito, A., Vanzi, M., 1988. A physically based mobility model for numerical simulation of nonplanar devices. IEEE Trans. Comput. Des. Integr. Circuits Syst. 7.

Martı, A., Balenzategui, J.L., Reyna, R.F., 1997. Photon recycling and Shockley's diode equation. J. Appl. Phys. 82 (8), 4067–4075.

Mearini, G.T., Krainsky, I.L., Dayton, J.a., Wang, Y., Zorman, C.A., Angus, J.C., Hoffman, R.W., 1994. Stable secondary electron emission observations from chemical vapor deposited diamond. Appl. Phys. Lett. 65 (21), 2702–2704.

Neamen, D.A., 2003. Semiconductor Physics and Devices: Basic Principles.

Nishioka, K., Takamoto, T., Agui, T., Kaneiwa, M., Uraoka, Y., Fuyuki, T., 2006. Evaluation of InGaP/InGaAs/Ge triple-junction solar cell and optimization of solar cell's structure focusing on series resistance for high-efficiency concentrator photovoltaic systems. Sol. Energy Mater. Sol. Cells 90, 1308–1321.

Rosenwaks, Y., Shapira, Y., Huppert, D., 1990. Metal reactivity effects on the surface recombination velocity at inp interfaces. Appl. Phys. Lett. 57 (24), 2552–2554.

Sahasrabuddhe, K., Schwede, J.W., Bargatin, I., Jean, J., Howe, R.T., Shen, Z.-X., Melosh, N.a., 2012. A model for emission yield from planar photocathodes based on photon-enhanced thermionic emission or negative-electron-affinity photoemission. J. Appl. Phys. 112 (9), 094907.

Sandovsky, R., 2015. Investigation of contact grid geometry for photon-enhanced thermionic emission (PETE) solar converters (M.Sc. Thesis). Tel Aviv University.

Schwede, J.W., Bargatin, I., Riley, D.C., Hardin, B.E., Rosenthal, S.J., Sun, Y., Schmitt, F., Pianetta, P., Howe, R.T., Shen, Z.-X., Melosh, N.A., 2010. Photon-enhanced thermionic emission for solar concentrator systems. Nat. Mater. 9, 762–767.

Schwede, J.W., Sarmiento, T., Narasimhan, V.K., Rosenthal, S.J., Riley, D.C., Schmitt, F., Bargatin, I., Sahasrabuddhe, K., Howe, R.T.,

Harris, Melosh, N.a., Shen, Z.-X., . Photon-enhanced thermionic emission from heterostructures with low interface recombination. Nat. Commun. 4 (January), 1576, 2013.
Segev, G., Rosenwaks, Y., Kribus, A., 2012. Efficiency of photon enhanced thermionic emission solar converters. Sol. Energy Mater. Sol. Cells 107, 125–130.
Segev, G., Rosenwaks, Y., Kribus, A., 2013. Loss mechanisms and back surface field effect in photon enhanced thermionic emission converters. J. Appl. Phys. 114 (4), 044505.
Segev, G., Weisman, D., Rosenwaks, Y., Kribus, A., 2015a. Negative space charge effects in photon-enhanced thermionic emission (PETE) solar converters. Appl. Phys. Lett. 107, 013908.
Segev, G., Rosenwaks, Y., Kribus, A., 2015b. Limit of efficiency for photon-enhanced thermionic emission vs. photovoltaic and thermal conversion. Sol. Energy Mater. Sol. Cells 140, 464–476.
Sze, S.M., Kwok, K.N., 2006. Physics of Semiconductor Devices, third ed. Wiley.
Van Kerschaver, E., Beaucarne, G., 2006. Back-contact solar cells: a review. Prog. Photovoltaics Res. Appl. 14 (2), 107–123.
Van Zeghbroeck, B., 2011. Principles of Electronic Devices (Chapter 2).
Varpula, A., Prunnila, M., 2012. Diffusion-emission theory of photon enhanced thermionic emission solar energy harvesters. J. Appl. Phys. 112 (4), 044506.
Weakliem, H.A., Redfield, D., 1979. Temperature dependence of the optical properties of silicon. J. Appl. Phys. 50, 1491.
Wurfel, P., 2005. Physics of Solar Cells from Principles to New Concepts. Wiley.